Volume 194 • July 2022

ISSN 0008-6223

ELSEVIER

Carbon

AN INTERNATIONAL JOURNAL

Reporting research on Carbonaceous Materials, their Production, Properties and Applications

EDITOR-IN-CHIEF: **M. Terrones**

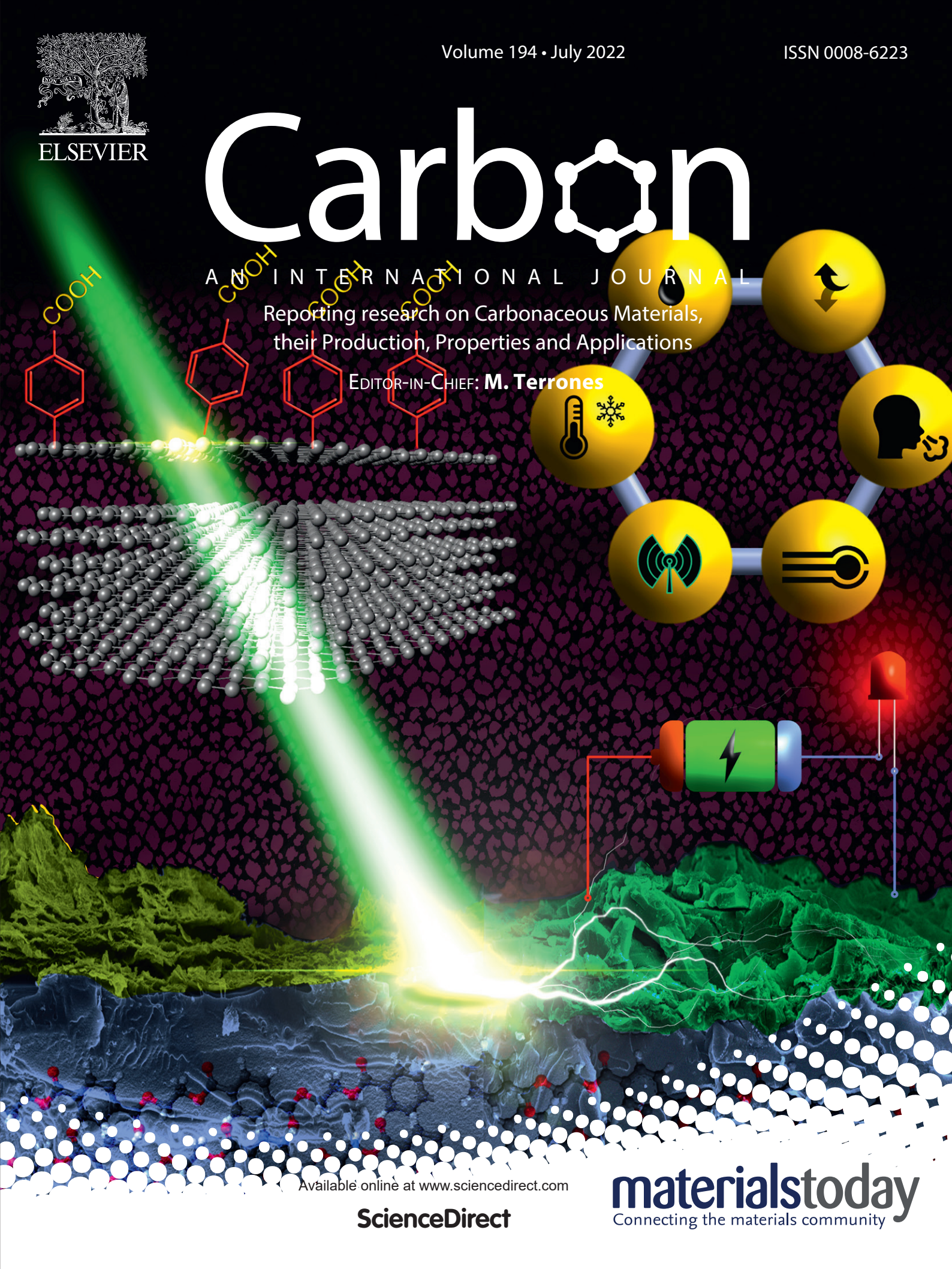

Available online at www.sciencedirect.com

ScienceDirect

materialstoday
Connecting the materials community

Carbon 194 (2022) 154–161

Contents lists available at ScienceDirect

Carbon

journal homepage: www.elsevier.com/locate/carbon

Photoinduced flexible graphene/polymer nanocomposites: Design, formation mechanism, and properties engineering

Anna Lipovka [a], Ilia Petrov [a], Maxim Fatkullin [a], Gennadiy Murastov [a], Alexey Ivanov [a], Nelson E. Villa [a], Sergey Shchadenko [a], Andrey Averkiev [a], Anna Chernova [a], Fedor Gubarev [a], Muhammad Saqib [a], Wenbo Sheng [b], Jin-Ju Chen [c], Olfa Kanoun [d], Ihsan Amin [e], Raul D. Rodriguez [a, *], Evgeniya Sheremet [a]

[a] Tomsk Polytechnic University, 30 Lenin Ave, 634050, Tomsk, Russia
[b] Chair of Macromolecular Chemistry, Faculty of Chemistry and Food Chemistry, School of Science, Technische Universität Dresden, 01069, Dresden, Germany
[c] School of Materials and Engineering, University of Electronic Science and Technology of China, 610054, Chengdu, China
[d] Chair of Measurement and Sensor Technology, Faculty of Electrical Engineering and Information Technology, Technische Universität Chemnitz, 09126 Chemnitz, Germany
[e] Van't Hoff Institute of Molecular Science, University of Amsterdam, Science Park 904, 1098XH, Amsterdam, the Netherlands

ARTICLE INFO

Article history:
Received 7 December 2021
Received in revised form
20 January 2022
Accepted 15 March 2022
Available online 25 March 2022

Keywords:
Graphene-based nanocomposites
Graphene
Laser processing
Sensor platform
Flexible electronics
Smart materials

ABSTRACT

Flexible electronics is a new paradigm with strong implications from healthcare to energy applications. In this context, electrically conductive polymers are the critical components. Here, we report the design, formation mechanism, and applications of a polymer nanocomposite obtained by single-step laser integration of functionalized graphene into a polymer matrix. Laser processing manipulates the physical-chemical properties of this nanocomposite in a controlled and straightforward way, tuning the electrical resistance from a dielectric (MΩ sq^{-1}) to a highly conductive material (Ω sq^{-1}). We combine experimental and computational approaches to elucidate graphene nanocomposite's nature and formation mechanism, evidencing different processes from photothermal polymer melting to shock wave mixing in a liquid phase within a millisecond time scale. We exploit these fundamental insights on the graphene/polymer nanocomposite in the design and fabrication of electrochemical sensing and antenna devices, showing the potential for healthcare and the Internet of Things.

1. Introduction

Conductive polymer nanocomposites are the emerging functional materials to face such challenges as lightweight flexible sensors, portable healthcare devices, batteries, and the Internet of Things. The synergetic effect of flexible polymer matrix and 2D conductive nanofiller modulates the crystallinity, mechanical robustness and electrical properties of the composite and offers an alternative for conventional conductive inks, flexible electronic components, and multifunctional sensors [1–4]. The most well-known approach to produce nanocomposites with improved properties is graphene/polymer integration [5–8]. The key feature is that both - polymers' chemistry and graphene's functionalization could be tailored.

The conventional routes to obtain bulk graphene/polymer mixtures with homogeneous flakes distributions include a solution or melt blending [4,9], and covalent grafting *via in situ* polymerization [10]. These approaches require modifying the whole matrix volume, while further structuring to form flexible devices involves extra steps. Instead, local selective treatment of the outermost surface is more cost-efficient for electronic applications. To this end, laser processing provides a brilliant opportunity to treat only the top layer of an already prepared polymer surface. Moreover, this photostructuring is mask-free, environmentally friendly, fast, scalable, and allows fabricating arbitrary patterns with a controllable spatial resolution [11,12].

The first way for laser processing of polymers involves high surface carbonization with the formation of so-called laser-induced graphene (LIG) [13,14]. By adjusting laser parameters, the optical, electrical, and wetting properties of LIG could be tuned [15–19].

* Corresponding author.
E-mail address: raul@tpu.ru (R.D. Rodriguez).

https://doi.org/10.1016/j.carbon.2022.03.039
0008-6223/

However, most laser wavelengths do not interact with transparent substrates, restricting LIG formation to only a few polymers. To overcome this, the integration of molecular or nanoparticle additives [20–23] is used to promote light absorption in an initially transparent polymer matrix such that subsequent photothermal conversion occurs. The second way to transfer graphene to other substrates is with laser-induced forward transfer (LIFT), which allows the use of solid or liquid materials as donors to perform LIG single-step deposition as voxels [24]. LIFT is promising for modern applications and leads to the composite formation, even though it could not be called straightforward as donor and acceptor polymers are required. The mechanical robustness of the material/substrate interaction obtained by LIFT was not yet reported.

In this work, we show the spatially selective laser integration of graphene into the surface of polymers to directly achieve a robust graphene/polymer composite. Compared with the state-of-the-art, we report a better alternative to bulk mixtures of the components or infiltration.

Earlier, we demonstrated that laser processing of graphene functionalized with diazonium salts (Mod-G) deposited as thin films on glass or Kapton enables the fabrication of highly conductive circuits [25]. By changing the substrate to polyethylene terephthalate (PET), we realized that laser processing reverses graphene functionalization and forms an extraordinary Mod-G/PET nanocomposite. In this work, we carefully investigated the underlying mechanisms behind the nanocomposite formation using experimental physical-chemical methods, high-speed imaging, and computer simulations that allow real-time visualization of the dynamics during laser-graphene-PET interaction. The new insights on laser processing of Mod-G significantly expand our understanding of this new technology to fabricate in a single-step electrically conductive polymer composites, decrease graphene consumption, and avoid the use of complicated power-hungry and costly equipment.

2. Materials and methods

2.1. Mod-G suspension fabrication and films deposition

The technology of Mod-G powder synthesis was kept as published in our previous work [25]. The obtained powder of functionalized graphene was further filtered and rinsed with water, ethanol, and acetone. Washed Mod-G was dried at ambient conditions. The powder was dispersed in either deionized water or ethanol following 4 mg/mL concentration and sonicated for 15 min. This concentration was selected in accordance with the one typically used for graphene oxide, which is the most common graphene form for the solution and laser processing of flexible electronics. Mod-G is an alternative to GO and for that reason we used 4 mg/mL. We kept this condition the same to make a more adequate comparison between these two graphene forms and their properties after laser treatment. Finally, the suspension was drop-casted on a PET substrate and dried in air. For comparison, we also prepared two more suspensions at concentrations of 2 mg/mL and 6 mg/mL (see Note S1, Fig. S1), and further focused on the original concentration, which is the most optimal according to our observations.

2.2. Laser treatment of Mod-G films

A 438 nm laser diode was used for direct patterning of specific geometry for the different sensors/applications. A laser power of ~500 mW was set as an optimal condition with respect to all types of sensors except chemical (~16.8 mW). The diameter of the laser beam at the focal point of the film surface was ~50 μm. For more detailed information see Note S1, in the Supporting Information (SI).

2.3. Characterization

Changes in the surface during laser processing were tracked by the high-speed imaging system (CuBr vapor brightness amplifier with a time resolution of 500 and 900 frames per second) [26]. The thickness of the nanocomposite was estimated by two methods of cross-section analysis: Scanning Electron Microscopy (SEM) using a Thermo Fisher Scientific Apreo S and optical microscopy. X-ray photoelectron spectroscopy (XPS) was measured on a Thermo Scientific K-Alpha system with an Al Kα X-ray source, with a spot size of 400 μm^2 and pass energies of 50 eV and 200 eV for narrow regions and survey spectra, respectively. TGA-DSC and TGA-MS analysis were performed using Q600 Simultaneous TGA–DTA analyzer (TA Instruments) coupled with VG ProLab quadrupole mass spectrometer (ThermoFisher Scientific) through a heated line (80 °C). TGA-DSC was carried out in an open alumina crucible under a dynamic argon atmosphere with a 100 mL/min flow rate, from ambient temperature to 1200 °C at a heating rate of 5 °C min^{-1}. The mass spectra were obtained under the electron impact ionization energy of 70 eV. Sheet resistance was obtained by two methods. First, measurements were done using the four-point probe method on a MS Tech MST 4000A microprobe station. The second method was Eddy Current Testing [27]. In order to investigate the wettability of Mod-G films and LMod-G/PET nanocomposites, the contact angle of a drop of distilled water was measured on the surface of the samples using the EasyDrop KRUSS device and drop shape analysis software (DSA). Finite element method (FEM) simulations of pulsed laser heating were performed employing the COMSOL Multiphysics software. More details on the characterization are described in the Supporting Information.

2.4. Sensor validation

Bending sensor performance was estimated using a three-point flexural test. The indenter movement was controlled by a microprocessor and a step motor. The bending diameters were 15, 20, 25, and 50 mm. The resistance measurements were obtained for every 10 bend-relax state cycles per constant diameter. The temperature sensor response was evaluated by the change in resistance of the sample from 80 °C to room temperature using a DS18B20 Waterproof temperature sensor chip. The reflection coefficient and voltage standing wave ratio results were obtained using the Agilent N22A PNA Network Analyzer at room conditions. For the evaluation of the resistance as a function of time for the chemical sensor, an Arduino ohm-meter was used. Skin conductance sensor testing was performed with 20 μL of NaCl water solution deposited on the clean dry pointer and middle fingers in contact with two LMod-G electrodes. The sensors' resistance was measured with a conventional multimeter. The electrochemical LMod-G sensor was tested in screen-printed electrode (SPE) configuration in 0.1 M aqueous solution of potassium ferrocyanide using Electrochemical Instruments P-45X potentiostat-galvanostat. For more information on validation see Supporting Information.

2.5. Antibacterial activity of LMod-G/PET

For antimicrobial assay three types of bacterial species were used: *Escherichia coli* (B-11333), *Staphylococcus aureus* (B-6646), Staphylococcus epidermidis (PCI 1200). All bacterial species were purchased from the Scientific Center "Kurchatov Institute" of the Research Institute for Genetics and Selection of Industrial Microorganisms. The bacteria were cultured on the following nutrient mediums: the Luria-Bertani medium for *E. Coli*, beef extract agar medium for *S. aureus*, and the MGYP agar medium for *S. epidermidis* at 37 °C for 18–24 h. The tested specimens were placed on Petri

dishes with 1% agar nutrient cultivating medium and inoculated with 0.2 ml of the microbial suspensions with a density of $1x10^8$ CFU/ml (according to 3 of McFarland scale). Then the Petri dishes with samples were incubated at 37 °C for 48 h. After incubation, the plates were checked for zones of inhibition of bacterial growth in transmitted light (More details of the antimicrobial assay in the Supporting Information).

3. Results and discussion

A robust, conductive, and flexible graphene/polymer nanocomposite was achieved by laser processing of Mod-G deposited on a PET surface (Fig. 1a, b, and 1c) since it is one of the most widely used polymers and has already shown an impressive combination with laser processing and graphene [28]. Mod-G was obtained following a recent report [25], by electrochemical exfoliation of a graphite electrode in 0.1 M sulfuric acid with 4-carboxybenzenediazonium tosylate (ADT-COOH) or 4-aminobenzenediazonium tosylate (ADT-NH_2). In the synthesis process, sulfate anions increase the carbon interlayer distance in graphite that, with simultaneous salt intercalation, results in efficient functionalization and exfoliation, as demonstrated previously [25]. The presence of $-NH_2$ or $-COOH$ functional groups significantly improves the dispersibility of graphene flakes making the solution processing straightforward and forming super-hydrophilic surfaces with a zero contact angle (CA) (Fig. S4, Supporting Information).

In contrast to conventional state-of-the-art approaches with nanofiller dispersed in the whole bulk polymer, the deposition of sufficiently homogeneous hydrophilic films is an essential factor to locally laser-pattern the graphene film on the polymer's surface. A related approach to process only the top layer was recently implemented using ink films for polymer marking [29], or reduced graphene oxide functionalization of carbon nanotubes covered polymer membranes for biosensing [30]. The critical process responsible for the final composite properties is the laser treatment of Mod-G (Fig. 2b) that induces several simultaneous processes discussed below (Fig. 1a). From now on, we denote the laser-treated Mod-G/polymer composite as LMod-G/PET (Fig. 1b). We found that the drastic structure modification induced by laser processing of Mod-G film promotes local PET melting with simultaneous LMod-G/PET composite formation (thickness is in the range 10–30 μm). This observation is evidenced by scanning electron microscopy (SEM) cross-section and optical microscopy images in Fig. 2a. Typically, laser irradiation of graphene (*i.e.;* GO) results in visible patterning and a more porous structure because of gas release, carbonization, and ablation [31]. That is also the case for laser treatment of electrochemically-exfoliated graphene without diazonium salts, as shown by SEM results in Fig. S5 (Supporting Information). However, the situation is entirely different for Mod-G that shows a smoother surface after laser processing (compare Fig. 2b and c). That is an indication of melted PET acting now as a matrix for graphene incorporation. This hypothesis is confirmed by energy-dispersive X-ray spectroscopy (EDX) results that show a decrease in carbon content and an increase of oxygen after laser processing (Fig. S6, Supporting Information), which agrees with SEM. X-ray photoelectron spectroscopy (XPS) results (Fig. 2d and e) support EDX revealing an initial carbon content of 81.0% with a minor change after irradiation (81.5%) and oxygen rise from 15.9% to 18.5%. Notably, the shape of XPS O1s and C1s high-resolution regions after laser processing become more PET-like, supporting our PET integration theory.

Even though the relative element content does not change significantly, laser treatment leads to significant changes in the molecular structure and chemical bonds, as shown by the C1s (285.0 eV) and O1s (532.0 eV) XPS regions. Untreated Mod-G film C1s region (Fig. 2d inset) was deconvoluted into three components attributed to C–C (284.5 eV), C–O (286.5 eV), and C=O (288.7 eV) bonds. Laser processing drives a sharp rise in the relative intensity of C=O, and to a lesser extent, the decrease in C–O one evidencing the change in polymer composition after patterning. Even the more drastic changes take place in the O1s region (532.4 eV) with the splitting of the oxygen-carbon peak into two closely-spaced peaks attributed to O=C (533.0 eV) and O–C (531.6 eV) bonds. This splitting reveals the presence of oxygen in two different chemical environments, which is compatible with the scenario of polymer coverage after laser-induced melting. The impact of functionalization is also illustrated in the XPS results of graphene obtained without diazonium salts (Fig. S7, Supporting Information). We see a significant rise in carbon content in this case, indicating that the top-layer surface does not contain melted PET.

In contrast to the smooth nanocomposite's outer surface, the inside of the layer is characterized by pores (Fig. 2a) caused by the intense gas release during laser processing. Similar pore formation

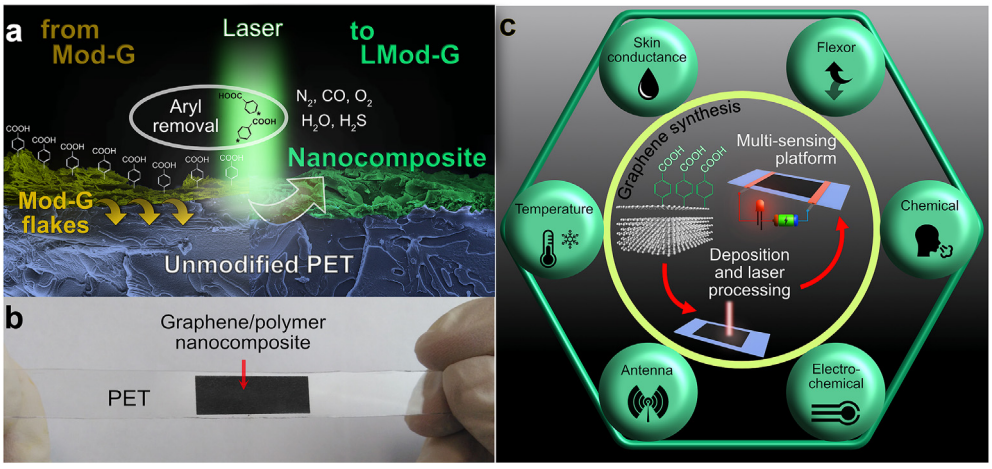

Fig. 1. Flexible and conductive graphene/polymer nanocomposite for implementation in sensors. a) Illustration of the composite formation mechanism with the different processes. Scanning electron microscopy cross-section images of Mod-G and LMod-G/PET showing the morphological and chemical changes. b) A photo of LMod-G/PET composite. c) Schematic illustration of LMod-G/PET composite fabrication process: from the synthesis of Mod-G to the fabrication of a versatile sensing platform using laser processing, and the demonstration of some applications developed in this work.

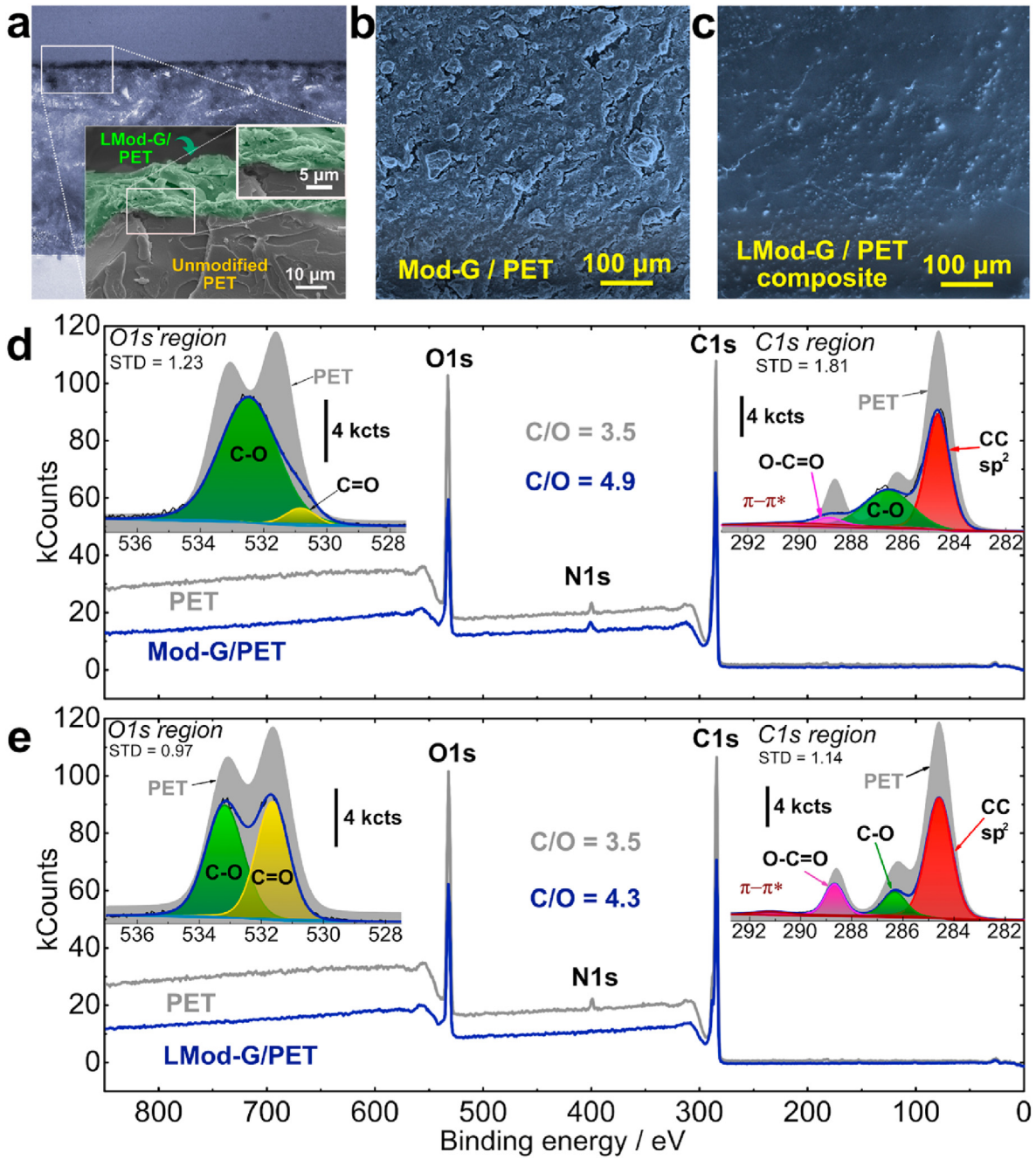

Fig. 2. Surface characterization of Mod-G/PET and LMod-G/PET. a) Optical and SEM cross-section images showing the composite formation. SEM images reveal the morphology of b) Mod-G film on PET, and c) LMod-G/PET composite. XPS survey spectra with O1s and C1s high-resolution regions (inset) of d) Mod-G/PET and pristine PET, and e) LMod-G/PET with bulk PET as a reference.

was previously observed after nano- and microsecond laser treatment with the occurrence of chemical reactions, bond openings, and phase transitions [32]. Studying the nature of the gases released during laser treatment helps to understand the mechanism of nanocomposite formation, inner processes during irradiation, and the nanocomposite composition. To this end, we qualitatively investigated the gas products content by gas mass spectrometry (MS) in the argon atmosphere to exclude the impact of air. Fig. S8 (Supporting Information) shows the results of mass spectrometry within the graphs divided into 3-time stages corresponding to (I) blanketing of argon atmosphere, (II) saturation, and (III) gas release during laser irradiation. The results show that the gaseous products include O_2, N_2, CO, H_2O, and H_2S as evidenced by the rise of these components during laser treatment of Mod-G film (Fig. S8a, Supporting Information).

O_2, CO, and H_2O are the expected ablation products, while H_2S comes as an electrolysis byproduct, with sulfur's presence confirmed by XPS and EDX. The XPS survey spectra of Mod-G film on the substrate reveal the widening of N1s peak compared to pure PET (Fig. 2d), confirming the successful diazonium functionalization of graphene that results in –N=N- groups. Nitrogen gets released by laser treatment which explains the disappearance of N1s peak in XPS (Fig. 2e). The unexpected finding is the absence of the CO_2 component in the mass spectra. This is surprising since

heating up to 460 °C must result in PET carbonization with solid carbon forms accompanied by CO_2, water, and H_2 release [33]. After considering different scenarios to explain this, and following previous reports for laser-reduced GO [34,35], we propose that the absence of CO_2 release is due to the graphene-mediated photocatalytic CO_2 reduction to CO: $CO_2 + 2H_2 + 2e^- \rightarrow CO + H_2O$.

To compare the photothermal laser-processing approach to conventional thermal annealing [36], we performed thermogravimetric-differential thermal analysis (TGA-DTA) combined with MS of Mod-G powder (Fig. S8b, Supporting Information) in the Ar atmosphere. Contrary to the laser treatment investigated by MS, in TGA-DTA we observe CO_2 and H_2O release above 150 °C due to −COOH decomposition with continuous weight reduction up to 1200 °C. The temperature rise above 1200 °C can explain these differences in gaseous products obtained by thermal annealing and laser processing during laser treatment or by a vital contribution of photochemical reactions expected for the violet laser we used (@438 nm). This second alternative implies that both photochemical and photothermal effects contribute significantly to the laser-induced LMod-G/PET composite formation.

The abrupt temperature rise in the area of the laser spot size (~50 μm) within tens μs per laser pulse provides heat transfer that induces local melting of the polymer in the presence of light absorption centers. State-of-the-art simulations show that in the process of laser patterning, the addition of impurities leads to a temperature rise in the PET matrix of up to 1000 °C for metallic absorbance centers and ~1475 °C for pristine graphene [37,38]. These temperatures are much higher than the PET melting point (~250 °C) [39]. The selective effect of laser patterning prompts an agile cooling system, slowing down the heat dissipation that leaves bulk PET unaffected while ensuring integration to the top layers.

To verify this hypothesis and optimize the material processing conditions, we performed finite element method (FEM) simulations of Mod-G/PET laser treatment. Fig. S9 (Supporting Information) shows a pulsed laser heating simulation of the Mod-G/PET with a set of power values covering a range representative of actual experiments. With the increase of laser power, we observe the temperature growth and the heat diffusion area over the sample. The most drastic temperature rise appears within the first second of laser-induced heating. Meanwhile, there is a noticeable decrease in the temperature for all powers used at the fifth second. This phenomenon is attributed to the pulsed nature of the laser load heat, as with continuous lasers, we expect a stable increase in the temperature over time. In simulations, the melting point of PET is firstly hit with 179 mW laser power at the first second of treatment when the temperature reaches 260 °C. At the third second, the highest temperature ~1250 °C is observed under a laser power of 542 mW.

Motivated by these simulation results, we fabricated samples using the same laser powers as in the computations to investigate how different temperatures contribute to the composite morphology. In Note S6 we correlate and discuss the temperatures reached after 1 s (since at this time occurs the most significant temperature rise and structural changes), optical images of the composite surface, and wetting properties (see Fig. S10, Supporting Information). Indeed, the laser power significantly contributes to the structure and surface properties that make different structural modifications accessible due to photothermal heating.

To see the laser-induced changes in real-time and evidence details that occur within the very first seconds and beyond, we recorded high-speed time-resolved videos (500 frames per second, fps) of the laser irradiation process in a single spot at different laser power values. This analysis clearly shows that PET starts melting within the first second of irradiation, for instance, using ~300 mW laser power (Video S1, Supporting). Then the area of melted polymer expands due to heat dissipation, and the temperature rises beyond the boiling point of PET (350 °C). These results correlate with our simulations that show the temperature values that could be reached in our experiments. Besides, we also performed high-speed video recording while scanning the laser over the sample with a speed of 5 mm/s (Video S2, Supporting Information). This video shows that the surface modification occurs *via* photothermal heat transfer in a liquid phase without PET boiling. More obviously, all these undergoing processes could be observed in the same experiments using a higher laser power (~450 mW). In this case, we examine surface changes characteristic of a shock wave (started from 0.01 s) and PET melting in the middle at the laser focus. After 0.3 s, the wave stops propagating, which means the equilibrium state is reached (Video S3, Supporting Information). Even with a fast laser scanning mode, graphene-PET modification can be obtained (Video S4, Supporting Information).

For flexible electronics, besides the essential control over structural and morphological characteristics, the control of electrical properties is critical [40]. Laser irradiation combining photothermal and photochemical effects promotes aryl groups' removal, resulting in electron delocalization and graphene restoration, turning the material to an effective electrical conductor [25]. Furthermore, the composite formation could be engineered to tune the electrical conductivity by adjusting laser parameters like the power. The laser power density controls the amount of atoms with hybridization state from sp^3 to sp^2 due to aryl functionalization removal and contributes to Mod-G ablation and the degree of its integration into the polymer. To demonstrate and implement this, we investigated the sheet resistance of untreated Mod-G film and chose two values of laser power used in our simulations (179 mW and 379 mW) for the real processing. For Mod-G, the sheet resistance of 18.45 ± 2.40 MΩ sq^{-1} indicates the effective functionalization of diazonium moieties, resulting in insulating properties. Laser processing with 179 mW power leads to a highly conductive composite with sheet resistance down to 30.03 Ω sq^{-1}. More interestingly, further increasing laser power leads to sheet resistance rise to 83 Ω sq^{-1}. The higher laser power values could even lead to a total loss of conductivity. TGA-DTA analysis in the air shows that the conductivity loss at the highest laser power is due to the extreme heat that results in Mod-G decomposition (Note S7, Fig. S11, Supporting Information). We associate the sheet resistance increase with interruption of the graphene conductive network by the non-conductive polymer matrix (Fig. S10, Supporting Information). We also show additional simulations for these two laser power values, including cross-section profiles and isothermal contours (Figs. S12 and S13, Supporting Information). We found that the electrical properties of our composites outperform laser-reduced GO films (see Table S1, Supporting Information) [15]. Additionally, even low-intensity laser irradiation with a laser power of 16.8 mW already leads to partial graphene structure restoration because of aryl removal. Under such mild conditions, there is no significant graphene incorporation into the polymer, but a resistance reduction from 10^6 to 10^3 range (13.6 ± 6.3 kΩ sq^{-1}) which is also useful for developing devices such as gas sensors.

Graphene, combined with other materials and functionalizations, is typically used to develop the latest sensors and catalysts [41]. Motivated by the potential that offers the graphene/polymer integration demonstrated above, we used LMod-G/PET to apply in antenna and electrochemical sensing (Fig. 3) and several more proof-of-principle devices shown in Note S11 (Supporting Information).

The fabrication of sensors with high sensitivity and selectivity for fast and reliable analysis is of uttermost importance for current and upcoming technologies. Electrochemical sensing meets the requirements mentioned above and offers easy integration in miniaturized devices [42]. For instance, electrochemical impedance

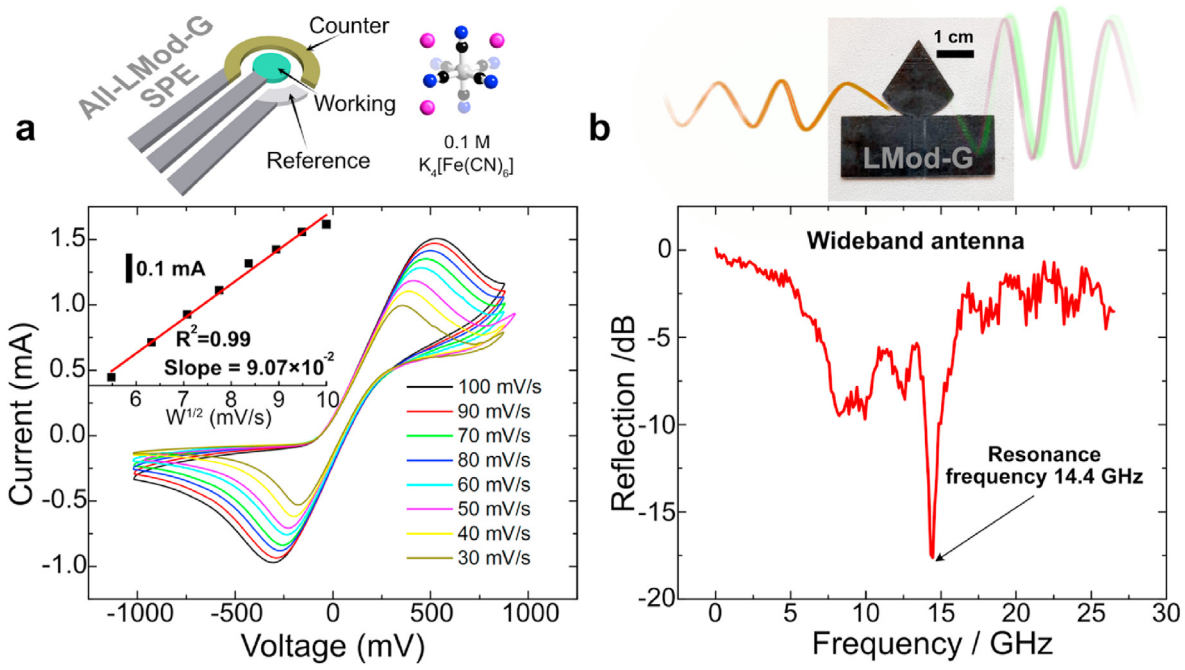

Fig. 3. LMod-G/PET as a multi-sensing platform a) Demonstration of electrochemical sensor behavior by CV-curves with the detection 0.1 M $K_4[Fe(CN)_6]$ at different scan rates. Inset shows the dependence of cathodic current peak to the square root of the scan rate. b) Reflection coefficient of LMod-G/PET cone inverted planar antenna with a photograph of the actual device.

spectroscopy (EIS) is promising for real-time biosensing [43]. We fabricated an LMod-G/PET-based electrochemical sensor with a standard screen-printed electrode (SPE) geometry to investigate our composite applicability in electrochemical sensing. We used potassium ferrocyanide ($K_4[Fe(CN)_6]$) as a model analyte system that is also widely used as a food additive. The obtained CVs show a characteristic cathodic peak due to the reduction of $[Fe(CN)_6]^{3-}$, and the anodic peak due to $[Fe(CN)_6]^{4-}$ oxidation following the reaction process on the electrode: $[Fe(CN)_6]^{3-} + e^- = [Fe(CN)_6]^{4-}$. Notably, the current values are above 1 mA in both regions, and the electrode shows stable behavior in a potential window from −1 to +1 V. We also investigated changes in CVs obtained while decreasing the diffused layer thickness by increasing the scan rate (from 30 to 100 mV s^{-1}). The curve's shape and peak current dependence from scan rate are in accordance with previous reports [44]. The scan rate increase also enhances matter flux. This effect no can be evaluated by plotting the peak intensity *vs.* the square root of the scan rate, as shown in the inset of Fig. 3a. The excellent linear fit with a coefficient of determination (COD) = 0.99 shows the fast dynamics of the reaction are not limited by charge transfer facilitated by the LMod-G electrode. Moreover, after detection, the sensor surface could be renewed by rinsing with distilled water or, if needed, electrochemically for further analysis with reusable characteristics.

Recently, carbon materials, including graphene, became the most promising candidates to overcome the limitation of poor mechanical flexibility and a tendency to corrosion typical for metal-based wireless communication antennas [45,46]. Thus, we designed and fabricated a miniaturized cone-planar waveguide antenna with a resonance frequency at 14.4 GHz, full-width-at-half-maximum of ~1 GHz, and a reflection coefficient of −18dB (Fig. 3b) [47]. Furthermore, the LMod-G-based Planar Inverted Cone Antenna (PICA) shows a voltage standing wave ratio (VSWR) of 1.8 and covers a wide bandwidth range from 7 to 17 GHz. These characteristics meet the requirements of wireless standards, including UWB communication [48].

Additionally, we successfully implemented LMod-G/PET for reusable and robust flexor, gas/breath sensor, electrothermal actuator, temperature, and skin resistance sensors (Note S11, Table S2, and Fig. S14, Supporting Information). Notably, gas sensors demonstrated a stable performance even after one year from the fabrication date, which indicates the long-term use and potential for mass production. This research may spark further developments in wireless charging and supercapacitor applications where the flexibility, stability, and surface conformation offered by this technology could be a game-changer. Considering all the options, our material enables the future development of a single multi-sensing platform, even expanding to wearables considering that the composite is not toxic and shows bacteriostatic behavior (Note S12, Supporting Information).

4. Conclusions

We report for the first time the laser-driven fabrication and formation mechanism behind a new type of graphene/polymer nanocomposite (LMod-G/PET) investigated by experimental physico-chemical methods, computer simulations, and real-time high-speed video recording. We showed that the laser pulse induces localized polymer melting and a shock wave in the liquid phase that promotes the integration of functionalized graphene into a conductive polymer-based framework. The absence of CO_2 release during laser processing by TGA points to a photocatalytic effect of functionalized graphene that could also play a role in the nanocomposite formation, while the release of CO and other gases explain the porous internal structure. Moreover, the tunable laser processing removes aryl groups resulting in electrical conductivity ranging from dielectric to metallic-like is particularly useful for electronic devices. We demonstrated that LMod-G/PET is an inexpensive and scalable alternative for flexible electrochemical sensors and antennas, and its bacteriostatic properties are prominent for future use in healthcare platforms, including wearables. Moreover, we have already investigated the implementation of LMod-G/

PET in temperature, breath/gas sensors, flexors, and skin conductance sensors. We consider the scalability of every engineering step that could make the fabrication technology commercially available and the high applicability of already fabricated sensors. Therefore, we foresee that the applications shown here are the tip of the iceberg of what could be done with this technology to engineer universal platforms for wearable sensors and flexible electronics.

CRediT authorship contribution statement

Anna Lipovka: Conceptualization, Methodology, Investigation, Validation, Formal analysis, Visualization, Supervision, Writing – original draft, Writing – review & editing. **Ilia Petrov:** Investigation, Visualization, Formal analysis, Validation, Writing – original draft. **Maxim Fatkullin:** Conceptualization, Methodology, Formal analysis, Validation, Writing – original draft, Writing – review & editing. **Gennadiy Murastov:** Methodology, Investigation, Formal analysis, Writing – original draft. **Alexey Ivanov:** Methodology, Investigation, Formal analysis, Writing – review & editing. **Nelson E. Villa:** Investigation, Formal analysis, Writing – review & editing. **Sergey Shchadenko:** Investigation, Formal analysis, Writing – review & editing. **Andrey Averkiev:** Investigation, Visualization, Formal analysis, Writing – review & editing. **Anna Chernova:** Investigation, Resources, Writing – review & editing. **Fedor Gubarev:** Conceptualization, Investigation, Writing – review & editing. **Muhammad Saqib:** Investigation, Formal analysis, Writing – original draft. **Wenbo Sheng:** Formal analysis, Writing – review & editing. **Jin-Ju Chen:** Investigation, Formal analysis, Writing – review & editing. **Olfa Kanoun:** Methodology, Writing – review & editing. **Ihsan Amin:** Formal analysis, Writing – original draft, Writing – review & editing. **Raul D. Rodriguez:** Conceptualization, Methodology, Visualization, Supervision, Writing – original draft, Writing – review & editing, Project administration. **Evgeniya Sheremet:** Validation, Supervision, Writing – original draft, Writing – review & editing, Resources, Funding acquisition, Project administration.

Declaration of competing interest

The authors declare that they have no known competing financial interests or personal relationships that could have appeared to influence the work reported in this paper.

Acknowledgments

This work was funded by RFBR and FWF research project No. 19-52-14006. The authors thank E. Sviridova and P. Postnikov for the synthesis of diazonium salts, E. Sevastyanov for the help with ethanol vapor detection, and V. Bogoslovskiy for the assistance during gas sensing and mass spectrometry experiments. We thank “MINATEH” company for the sheet resistance measurements. We are also grateful to A. Al-Hamry and D. Rajendran for their help with antenna characterization. This research was supported by the TPU development program. JJC acknowledges the Sichuan Science and Technology Program [grant number 2018HH0152]. The research was carried out using the core facilities of TPU's “Physics and Chemical methods of analysis”.

Appendix A. Supplementary data

Supplementary data to this article can be found online at https://doi.org/10.1016/j.carbon.2022.03.039.

References

[1] D. Ponnamma, Q. Guo, I. Krupa, M.A.S.A. Al-Maadeed, S. Thomas, K.K. Sadasivuni, Graphene and graphitic derivative filled polymer composites as potential sensors, Phys. Chem. Chem. Phys. 17 (2015) 3954–3981.
[2] L. Nayak, S. Mohanty, S.K. Nayak, A. Ramadoss, A review on inkjet printing of nanoparticle inks for flexible electronics, J. Mater. Chem. C 7 (2019) 8771–8795, https://doi.org/10.1039/c9tc01630a.
[3] X. Sun, C. Huang, L. Wang, L. Liang, Y. Cheng, W. Fei, Y. Li, Recent progress in graphene/polymer nanocomposites, Adv. Mater. 33 (2021), e2001105.
[4] A. Noël, J. Faucheu, M. Rieu, J.-P. Viricelle, E. Bourgeat-Lami, Tunable architecture for flexible and highly conductive graphene–polymer composites, Compos. Sci. Technol. 95 (2014) 82–88, https://doi.org/10.1016/j.compscitech.2014.02.013.
[5] A.D. de Oliveira, A.D. de Oliveira, C.A.G. Beatrice, Polymer Nanocomposites with Different Types of Nanofiller, Nanocomposites - Recent Evolutions, 2019, https://doi.org/10.5772/intechopen.81329.
[6] T. Zhang, R.D. Rodriguez, I. Amin, J. Gasiorowski, M. Rahaman, W. Sheng, J. Kalbacova, E. Sheremet, D.R.T. Zahn, R. Jordan, Bottom-up fabrication of graphene-based conductive polymer carpets for optoelectronics, J. Mater. Chem. C 6 (2018) 4919–4927, https://doi.org/10.1039/c8tc00554k.
[7] Q. Yang, Z. Zhang, X. Gong, E. Yao, T. Liu, Y. Zhang, H. Zou, Thermal conductivity of Graphene-polymer composites: implications for thermal management, Heat Mass Tran. 56 (2020) 1931–1945.
[8] W. Gao, N. Zhao, T. Yu, J. Xi, A. Mao, M. Yuan, H. Bai, C. Gao, High-efficiency electromagnetic interference shielding realized in nacre-mimetic graphene/polymer composite with extremely low graphene loading, Carbon N. Y. 157 (2020) 570–577.
[9] B. Yuan, C. Bao, L. Song, N. Hong, K.M. Liew, Y. Hu, Preparation of functionalized graphene oxide/polypropylene nanocomposite with significantly improved thermal stability and studies on the crystallization behavior and mechanical properties, Chem. Eng. J. 237 (2014) 411–420, https://doi.org/10.1016/j.cej.2013.10.030. W. Gao, N. Zhao, T. Yu, J. Xi, A. Mao, M. Yuan, H. Bai, C. Gao.
[10] Z. Xu, C. Gao, In situPolymerization approach to graphene-reinforced nylon-6 composites, Macromolecules 43 (2010) 6716–6723, https://doi.org/10.1021/ma1009337.
[11] R.D. Rodriguez, G.V. Murastov, A. Lipovka, M.I. Fatkullin, O. Nozdrina, S.K. Pavlov, P.S. Postnikov, M.M. Chehimi, J.-J. Chen, E. Sheremet, High-power laser-patterning graphene oxide: a new approach to making arbitrarily-shaped self-aligned electrodes, Carbon N. Y. 151 (2019) 148–155.
[12] L. Mühlenbein, C.B. Singh, A. Lotnyk, C. Himcinschi, Y. Yun, N. Ramakrishnegowda, D.S. Knoche, X. Li, A. Bhatnagar, Nanocomposites with three-dimensional architecture and impact on photovoltaic effect, Nano Lett. 20 (2020) 8789–8795.
[13] R. Ye, D.K. James, J.M. Tour, Laser-induced graphene: from discovery to translation, Adv. Mater. 31 (2019), e1803621.
[14] L. Groo, J. Nasser, D.J. Inman, H.A. Sodano, Transfer printed laser induced graphene strain gauges for embedded sensing in fiberglass composites, Compos. B Eng. 219 (2021) 108932, https://doi.org/10.1016/j.compositesb.2021.108932.
[15] Z. Wan, E.W. Streed, M. Lobino, S. Wang, R.T. Sang, I.S. Cole, D.V. Thiel, Q. Li, Laser-reduced graphene: synthesis, properties, and applications, Adv. Mater. Technol. 3 (2018) 1700315, https://doi.org/10.1002/admt.201700315.
[16] L. Cao, S. Zhu, Z.B. Pan, X. Dai, W. Zhao, Y. Liu, W. Xie, Y. Kuang, X. Liu, Stable and durable laser-induced graphene patterns embedded in polymer substrates, Carbon N. Y. 163 (2020) 85–94.
[17] A. Dallinger, K. Keller, H. Fitzek, F. Greco, Stretchable and skin-conformable conductors based on polyurethane/laser-induced graphene, ACS Appl. Mater. Interfaces 12 (2020) 19855–19865.
[18] R. You, Y.-Q. Liu, Y.-L. Hao, D.-D. Han, Y.-L. Zhang, Z. You, Laser fabrication of graphene-based flexible electronics, Adv. Mater. 32 (2020), e1901981.
[19] H. Yao, P. Li, W. Cheng, W. Yang, Z. Yang, H.P.A. Ali, H. Guo, B.C.K. Tee, Environment-resilient graphene vibrotactile sensitive sensors for machine intelligence, ACS Mater. Lett. 2 (2020) 986–992, https://doi.org/10.1021/acsmaterialslett.0c00160.
[20] R.D. Rodriguez, S. Shchadenko, G. Murastov, A. Lipovka, M. Fatkullin, I. Petrov, T. Tran, A. Khalelov, M. Saqib, N.E. Villa, V. Bogoslovskiy, Y. Wang, C. Hu, A. Zinovyev, W. Sheng, J. Chen, I. Amin, E. Sheremet, Ultra-robust flexible electronics by laser-driven polymer-nanomaterials integration, Adv. Funct. Mater. 31 (2021) 2008818, https://doi.org/10.1002/adfm.202008818.
[21] W. Zhong, Z. Cao, P. Qiu, D. Wu, C. Liu, H. Li, H. Zhu, Laser-marking mechanism of thermoplastic polyurethane/Bi2O3 composites, ACS Appl. Mater. Interfaces 7 (2015) 24142–24149.
[22] C. Zhang, Y. Dai, G. Lu, Z. Cao, J. Cheng, K. Wang, X. Wen, W. Ma, D. Wu, C. Liu, Facile fabrication of high-contrast and light-colored marking on dark thermoplastic polyurethane materials, ACS Omega 4 (2019) 20787–20796.
[23] K.S. Zelenska, S.E. Zelensky, L.V. Poperenko, K. Kanev, V. Mizeikis, V.A. Gnatyuk, Thermal mechanisms of laser marking in transparent polymers with light-absorbing microparticles, Opt Laser. Technol. 76 (2016) 96–100, https://doi.org/10.1016/j.optlastec.2015.07.011.

[24] P. Serra, A. Piqué, Laser-induced forward transfer: fundamentals and applications, Adv. Mater. Technol. 4 (2019) 1800099, https://doi.org/10.1002/admt.201800099.
[25] R.D. Rodriguez, A. Khalelov, P.S. Postnikov, A. Lipovka, E. Dorozhko, I. Amin, G.V. Murastov, J.-J. Chen, W. Sheng, M.E. Trusova, M.M. Chehimi, E. Sheremet, Beyond graphene oxide: laser engineering functionalized graphene for flexible electronics, Mater. Horiz. 7 (2020) 1030–1041, https://doi.org/10.1039/c9mh01950b.
[26] L. Li, D.V. Shiyanov, F.A. Gubarev, Spatial–temporal radiation distribution in a CuBr vapor brightness amplifier in a real laser monitor scheme, Appl. Phys. B 126 (2020), 155, https://doi.org/10.1007/s00340-020-07511-7.
[27] S. Huang, S. Wang, New Technologies in Electromagnetic Non-destructive Testing, Springer (2016).
[28] A. Kamyshny, S. Magdassi, Conductive nanomaterials for 2D and 3D printed flexible electronics, Chem. Soc. Rev. 48 (2019) 1712–1740.
[29] P. Chang, A. Bruntz, L. Vidal, P. Vetter, P. Roudot, L. Bua, J. Ortiz, H. Zan, O. Soppera, Laser polymer tattooing: a versatile method for permanent marking on polymer surfaces, Macromol. Mater. Eng. 304 (2019) 1900402, https://doi.org/10.1002/mame.201900402.
[30] J. Barkauskas, L. Mikoliunaite, I. Paklonskaite, P. Genys, J.J. Petroniene, I. Morkvenaite-Vilkonciene, A. Ramanaviciene, U. Samukaite-Bubniene, A. Ramanavicius, Single-walled carbon nanotube based coating modified with reduced graphene oxide for the design of amperometric biosensors, Mater. Sci. Eng. C Mater. Biol. Appl. 98 (2019) 515–523.
[31] Y.C. Guan, Y.W. Fang, G.C. Lim, H.Y. Zheng, M.H. Hong, Fabrication of laser-reduced graphene oxide in liquid nitrogen environment, Sci. Rep. 6 (2016) 28913.
[32] A. Royon, Y. Petit, G. Papon, M. Richardson, L. Canioni, Femtosecond laser induced photochemistry in materials tailored with photosensitive agents [Invited], Opt. Mater. Express 1 (2011) 866, https://doi.org/10.1364/ome.1.000866.
[33] A.R. Kamali, J. Yan, Effect of molten salts on the structure, morphology and electrical conductivity of PET-derived carbon nanostructures, Polym. Degrad. Stabil. 177 (2020) 109184.
[34] X. Li, J. Wen, J. Low, Y. Fang, J. Yu, Design and fabrication of semiconductor photocatalyst for photocatalytic reduction of CO2 to solar fuel, Sci. China Mater. 57 (2014) 70–100, https://doi.org/10.1007/s40843-014-0003-1.
[35] Y. Kuang, J. Shang, T. Zhu, Photoactivated graphene oxide to enhance photocatalytic reduction of CO2, ACS Appl. Mater. Interfaces 12 (2020) 3580–3591, https://doi.org/10.1021/acsami.9b18899.
[36] G.T.T. Le, J. Manyam, P. Opaprakasit, N. Chanlek, N. Grisdanurak, P. Sreearunothai, Divergent mechanisms for thermal reduction of graphene oxide and their highly different ion affinities, Diam. Relat. Mater. 89 (2018) 246–256, https://doi.org/10.1016/j.diamond.2018.09.006.
[37] L. Wen, T. Zhou, J. Zhang, A. Zhang, Local controllable laser patterning of polymers induced by graphene material, ACS Appl. Mater. Interfaces 8 (2016) 28077–28085.
[38] Y. Farazila, YAG laser spot welding of PET and metallic materials, J. Laser Micro/Nanoeng. 6 (2011) 69–74, https://doi.org/10.2961/jlmn.2011.01.0015.
[39] L. Wang, Y. Wang, F. Zhang, Y. Bai, L. Ding, Syntheses and properties of the PET- co -PEA copolyester : article, J. Appl. Polym. Sci. 134 (2017) 44967.
[40] J.M. Lee, G. Hong, D. Lin, T.G. Schuhmann Jr., A.T. Sullivan, R.D. Viveros, H.-G. Park, C.M. Lieber, Nanoenabled direct contact interfacing of syringe-injectable mesh electronics, Nano Lett. 19 (2019) 5818–5826.
[41] M. Baitimirova, R. Viter, J. Andzane, A. van der Lee, D. Voiry, I. Iatsunskyi, E. Coy, L. Mikoliunaite, S. Tumenas, K. Załęski, Z. Balevicius, I. Baleviciute, A. Ramanaviciene, A. Ramanavicius, S. Jurga, D. Erts, M. Bechelany, Tuning of structural and optical properties of graphene/ZnO nanolaminates, J. Phys. Chem. C Nanomater. Interfaces 120 (2016) 23716–23725.
[42] Y.-N. Zhang, Q. Niu, X. Gu, N. Yang, G. Zhao, Recent progress on carbon nanomaterials for the electrochemical detection and removal of environmental pollutants, Nanoscale 11 (2019) 11992–12014.
[43] I. Morkvenaite-Vilkonciene, P. Genys, A. Ramanaviciene, A. Ramanavicius, Scanning electrochemical impedance microscopy for investigation of glucose oxidase catalyzed reaction, Colloids Surf. B Biointerfaces 126 (2015) 598–602.
[44] V.V. Shumyantseva, T.V. Bulko, A.V. Kuzikov, R. Khan, A.I. Archakov, Development of methods for functionalization of screen printed electrodes with biocompatible organic-inorganic hybrid nanocomposites for biosensing applications, Biochem. (Moscow) Suppl. B: Biomed. Chem. 8 (2014) 237–242, https://doi.org/10.1134/s1990750814030123.
[45] A. Nag, S.C. Mukhopadhyay, J. Kosel, Wearable flexible sensors: a review, IEEE Sensor. J. 17 (2017) 3949–3960, https://doi.org/10.1109/jsen.2017.2705700.
[46] C. Reig, E. Avila-Navarro, Printed antennas for sensor applications: a review, IEEE Sensor. J. 14 (2014) 2406–2418, https://doi.org/10.1109/jsen.2013.2293516.
[47] A. Alomainy, Y. Hao, Radio channel models for UWB body-centric networks with compact planar antenna, in: 2006 IEEE Antennas and Propagation Society International Symposium, 2006, https://doi.org/10.1109/aps.2006.1711017.
[48] A. Alomainy, Y. Hao, C.G. Parini, P.S. Hall, Comparison between two different antennas for UWB on-body propagation measurements, IEEE Antenn. Wireless Propag. Lett. 4 (2005) 31–34, https://doi.org/10.1109/lawp.2005.844143.